Mineral replacement rate of olivine by chrysotile and brucite under high alkaline conditions

Romain Lafay [a,*], German Montes-Hernandez [a,*], Emilie Janots [a], Rodica Chiriac [b], Nathaniel Findling [a], Francois Toche [b]

[a] Institut des Sciences de la Terre (ISTerre), UJF-CNRS, F-38041, Grenoble I, Cedex 9, France
[b] Université Lyon 1, Laboratoire des Multimatériaux et Interfaces UMR CNRS 5615, 43 bd du 11 novembre 1918, 69622 Villeurbanne Cedex, France

ABSTRACT

Olivine mineral replacement by serpentine is one major alteration reaction of oceanic hydrothermalism. In the present experimental study, olivine grains were replaced by chrysotile and brucite under high alkaline conditions. In our study, olivine replacement implied a spatial and temporal coupling of dissolution and precipitation reactions at the interface between olivine and chrysotile–brucite minerals. Coupled dissolution–precipitation led to the alteration of starting olivine grains (so-called primary or parent mineral) to a porous mineral assemblage of chrysotile and brucite with preservation of the initial olivine morphology. This mineral replacement reaction of olivine (serpentinization) has been characterized using XRD, FESEM and FTIR measurements. Moreover, a simple and novel method is here proposed to quantify the mineral replacement rate (or serpentinization rate) of olivine using thermogravimetric (TG) and differential TG (DTG) analyses. Serpentinization extent depends on the grain size: it is complete after 30 days of reaction for the smallest olivine grains ($< 30\,\mu m$), after 90 days of reaction for the intermediate olivine grains ($30\,\mu m$–$56\,\mu m$). For the largest fraction (56–$150\,\mu m$), 55% of serpentinization extent was reached after 90 days. Based on the fitting of the serpentinization extent (ξ_t) versus time (t) using a kinetic pseudo-second-order model, the serpentinization rates vary from $3.6 \times 10^{-6}\,s^{-1}$ to $1.4 \times 10^{-7}\,s^{-1}$ depending on the olivine grain size. An additional correlation between FTIR spectra analysis and TG measurements is proposed. The mineral replacement reactions frequently observed in natural alteration processes could be a powerful synthesis route to design new porous and/or nanostructured materials.

© 2012 Elsevier B.V. All rights reserved.

1. Introduction

Serpentine minerals (chrysotile, lizardite and antigorite) are widespread in Earth's oceanic lithosphere and are frequently found in chondrites and other extraterrestrial objects. Serpentine mineralization is of great interest in several fields of research. Serpentinized rocks present a great enrichment in trace elements compared to primary mantle rocks [1–6]. Serpentine appears as a vector for trace elements between crustal and mantle reservoirs [2,5,7,8]. Experimental studies have tested the influence of major–minor (e.g. Fe, Ni) and/or trace elements (e.g. Li) on the growth of serpentine [9–14]. This kind of synthesis experiments presents a great interest in medical research due to the asbestos toxicity that can be induced by inhalation of magnesium silicates' fibers including chrysotile [15–18]. Serpentine minerals are also crucial for sequestration of CO_2 due to its availability and sequestration capacity [19–21]. Indeed a lot of studies are looking for technologies that could possibly contribute to reduce carbon dioxide emissions. Geological sequestration and ex-situ mineralization of CO_2 using serpentine could be one of the most efficient methods considering the enormous quantity of serpentine on Earth [22].

In meteorites, serpentine minerals are directly linked to aqueous alteration processes and reaction conditions (e.g. [23] and references therein). In the oceanic lithosphere, serpentines result from interaction between mantle rocks (peridotite composed by olivine and pyroxenes) and hydrothermal fluids, generally with high fracturation dynamic [24,25]. Olivine alters along grain boundaries and fractures to produce a mesh texture that preserves the original olivine morphology at the grain scale [26,27]. This olivine replacement by serpentine is best explained by coupled dissolution–precipitation processes [28–30]. This re-equilibration process leads to the replacement of one pristine mineral by a secondary mineral (or assemblage) with a lower solubility in the fluid. Replacement occurs at the fluid/solid

---

interface maintaining the original external grain shape (pseudo-morphism). During alteration, a secondary porosity is commonly produced due to volume difference between pristine and secondary minerals, material loss during dissolution and grain fracturation [24,25]. Secondary porosity enables the fluid to move interstitially towards the reaction front until the complete mineral replacement reaction. In oceanic lithosphere, peridotite replacement, and consequent element redistribution associated with this alteration, is primarily controlled by the physico-chemical conditions of the hydrothermal fluid (temperature, pressure, fluid speciation, and pH). Fluids escaping from deep sea hydrothermal vents show a large variety of composition and pH, reflecting a large range of possible physico-chemical conditions. Amongst them, alkaline fluids with high pH were collected in some hydrothermal fields (e.g., [31,32]).

Numerous experimental studies were conducted to reproduce serpentinization in hydrothermal context [33–40, 54] and explain serpentine growth [41]. Kinetic appears faster under alkaline conditions [40,42] but few recent studies have addressed the role of pH on serpentinization kinetic, particularly in alkaline conditions.

In the present experimental study, we have investigated the process and kinetics of olivine serpentinization in alkaline hydrothermal conditions (pH=13.5, measured at 25 °C). Experimental products were characterized using XRD, FESEM and FTIR. The serpentinization rate was determined using a simple and novel method based on thermogravimetric analyses (TGA/DTGA). This demonstrates that serpentinization is much faster under alkaline conditions referring to previous studies at comparable conditions [35,36,43] and can lead to a total replacement of $< 30\,\mu m$ olivine in less than 30 days and 90 days for $30 <$ particle size $< 56\,\mu m$.

2. Materials and methods

Millimetric grains of olivine San Carlos (Fo_{91}) were crushed using a Fritsh Pulverisette 7 micro-crusher. Three classes of grain/particle size (particle size $< 30\,\mu m$, $30 <$ particle size $< 56\,\mu m$ and $56 <$ particle size $< 150\,\mu m$) were isolated by sieving. The samples were washed three times using high-pure water in order to remove the ultrafine particles that possibly stuck at grain surfaces during crushing step. Optical and electron microscopy was performed to control the initial state/appearance of olivine surfaces.

2.1. Alteration experiments

1.5 ml of high alkaline solution (1 M of NaOH, pH ≈ 13.5 at 25 °C) and 100 mg of San Carlos olivine at a given class of particle size were placed in a Teflon cell reaction (cap-cell also in Teflon). Cell reaction and cap-cell were previously washed by an acidic treatment followed by washing with high-pure water. This cell reaction was immediately assembled into a steel autoclave without agitation, referred to as "static batch reactor" and the closed autoclave was placed in a multi-oven (ten independent-temperature compartments) and heated to 150 °C or 200 °C ($P_{sat} \sim 0.5$ Mpa and $P_{sat} \sim 1.6$ Mpa). Various olivine–alkaline solution reaction times from 3 h to 90 days were considered in order to determine the mineral replacement rate (or serpentinization rate) of olivine at the investigated hydrothermal conditions. Particularly, the effect of initial particle size (three different classes: particle size $< 30\,\mu m$, $30 <$ particle size $< 56\,\mu m$ and $56 <$ particle size $< 150\,\mu m$) on the serpentinization rate of olivine was tested. All experimental conditions are summarized in Table 1.

At the end of the experiment, the autoclave was quenched in cold water. This manipulation avoids precipitation during cooling with no perturbation of the reaction products. Then, the autoclave was disassembled and the fluid was collected for pH and major elements concentration (Mg, Fe and Si) measurements (not shown in this study). After all experiments, pH of the experimental fluid is still around 13.5 (measured at 25 °C). The solid product was dried directly in the Teflon cell at 80 °C for 24 h. The dry solid product was recovered for further solid characterizations described below.

2.2. X-Ray diffraction measurements

X-Ray diffraction (XRD) analyses were performed in the ISTerre laboratory. All samples were crushed manually. The powders were carefully placed and manually compacted in

Table 1
Summary of the experimental conditions.

Run no.	T (°C)	Time	Grain size (μm)	Olivine to Chrysotile conversion (%)	Alteration products
1	200	3 h	< 30	10.3	O > C > B
2	200	16 h	< 30	21.7	O > C > B
3	200	24 h	< 30	24.6	O > C > B
4	200	48 h	< 30	37.5	O > C > B
5	200	72 h	< 30	51.7	O ≈ C > B
6	200	10 d	< 30	73.8	C > O > B
7	200	20 d	< 30	88.8	C > B > O
8	200	30 d	< 30	98.0	C > B
9	200	90 d	< 30	98.2	C > B
10	150	30 d	< 30	49.5	O ≈ C > B
11	150	66 d	< 30	Not determined	C > O > B
12	200	3 d	30–56	19.6	O > C > B
13	200	10 d	30–56	26.2	O > C > B
14	200	24 d	30–56	46.2	O ≈ C > B
15	200	41 d	30–56	77.1	C > O > B
16	200	51 d	30–56	71.1	C > O > B
17	200	72 d	30–56	88.9	C > B > O
18	200	90 d	30–56	94.4	C > B > O
19	200	13 d	56–150	10.7	O > C > B
20	200	32 d	56–150	26.6	O > C > B
21	200	60 d	56–150	44.2	O > C > B
22	200	90 d	56–150	55.4	C > O > B

All experiments have been performed at pH 13.5 (measured at 25 °C). Saturated pressure is constant: 1.6 MPa for 200 °C and 0.5 MPa for 150 °C reactions. Fluid/rock ratio is always ∼15. O: olivine, C: chrysotile, and B: brucite.

borosilicated capillaries of 500 μm of diameter, this corresponds to about 5 mg of sample. XRD patterns were recorded with a Bruker D8 powder diffractometer equipped with a SolX Si (Li) solid state detector from Baltic Scientific Instruments using CuKα1–Kα2 radiation and a Göbel mirror. Intensities were recorded for 2θ interval from $5°$ to $80°$ with an 8 s counting time per $0.024°$ 2θ step for bulk mineralogy determination.

2.3. FESEM observations

Grain size and morphology of the experimental products were characterized using secondary or backscattered electrons. Micro-imaging was obtained using Zeiss Ultra 55 Field emission gun scanning electron microscopy (FESEM). This enables a spatial resolution of approximately 1 nm at 15 kV. Samples were dispersed by ultrasonic treatment in absolute ethanol for at least 5 min in order to disaggregate the particles. One or two drops of dispersion were placed onto an aluminum support and coated with a thin film of platinum for FESEM observation.

2.4. Thermogravimetric analyses (TGA)

TGA for experimental solid products were performed with a TGA/SDTA 851^{e}Mettler Toledo instrument under the following conditions: sample mass of about 10 mg, platine crucible of 150 μl with a pinhole, heating rate of $10\ °C\ min^{-1}$, and inert N_2 atmosphere of $50\ ml\ min^{-1}$. Sample mass loss and associated thermal effects were obtained by TGA/DTGA in a temperature range from $30\ °C$ to $1200\ °C$. In order to identify the different mass loss steps, the TGA first derivative (rate of mass loss) was used. TGA apparatus was calibrated in terms of mass and temperature. Calcium oxalate was used for the sample mass calibration. The melting points of three compounds (indium, aluminum and copper) obtained from the SDTA signals were used for the sample temperature calibration. The temperature accuracy of the TGA/SDTA system is about $\pm 0.25\ °C$. The weighting accuracy is around 0.1 μg, which correspond to 0.001% for a 10 mg sample.

2.5. FTIR measurements

FTIR measurements (in transmission mode) were performed using an IR microscope Bruker Hyperion 3000. The IR beam was focused through a 15x lens and the typical size of infrared spot is $50 \times 50\ \mu m^2$. The light source is a Globar (TM) and the beam splitter is in KBr. The spectra were measured from 700 to $4000\ cm^{-1}$ ($4\ cm^{-1}$ resolution) with a MCT monodetector cooled by liquid nitrogen.

Samples must be thin (less than 100 μm) and flat to avoid absorption band saturation or scattering effects. Sample preparation has involved a careful crushing of samples in mortar and manual compaction of fine crushed particles between two K–Br windows. Five spectra per samples were realized; they were fitted using OPUS software.

3. Results and discussion

3.1. Serpentinization reaction under alkaline conditions

Secondary minerals were identified by XRD and FESEM (Figs. 1 and 2) and they were quantified by TGA (Fig. 3). Under alkaline conditions, olivine is replaced by chrysotile and brucite, independently on the starting grain size of olivine. No other minerals were detected and/or observed during this alteration reaction.

FESEM micro-imaging has revealed a clear evolution of particle size and morphology of crystal faces during serpentinization advancement (Fig. 2). Serpentine nucleation at olivine–alkaline solution interfaces is observable by FESEM after only few hours of reaction when the starting grain size is $< 30\ \mu m$ (Fig. 2a). These occur as nanosized nodules forming irregular sub-micrometric rods. They are still observed on olivine surfaces after few days of reaction and a more advanced serpentinization reaction (Fig. 2c). The irregular sub-micrometric rods were identified as chrysotile and brucite "clusters" from TGA/DTGA in the solid product (Fig. 3). While brucite is detected by XRD in the first stages of replacement (e.g. 3 h of reaction for $< 30\ \mu m$ grains), chrysotile was not detected by XRD, possibly due to its poor crystallinity and/or nanometric size. Chrysotile was detected by XRD after 16 h of reaction for the smallest starting grains ($< 30\ \mu m$), however, several days of olivine–fluid interactions are required when the starting grain size is $> 30\ \mu m$ (Fig. 1a and b). At advanced alteration stages, serpentinized samples consist of tubular, conical and cylinder-in-cylinder chrysotile with nanometric diameter and microsized hexagonal brucite were clearly observed (Fig. 2e, g, and h). Diameter of secondary products depends on the starting material grain size. It increases from $\sim 50\ nm$ for the $< 30\ \mu m$, to $200–300\ nm$ for $30–56\ \mu m$ and $56–150\ \mu m$ fractions. Lizardite was not observed. Previous studies suggested that lizardite crystallized at lower levels of supersaturation than chrysotile e.g. [44]. Here, we confirm that high alkaline pH favors chrysotile precipitation [40,42].

In natural samples, olivine replacement in mesh texture is commonly described as an assemblage of serpentine $\pm$ brucite $\pm$ magnetite. Typically, the magnetite amount depends on the Mg# (Mg#=Mg/(Mg+Fe)) in primary olivine. Neither iron oxides (e.g. magnetite or hematite) nor oxyhydroxides (e.g. goethite) were observed in our experiments. Semi-quantitative EDS analyses have revealed that the initial iron contained in olivine was preferentially incorporated as Fe^{2+} into brucite (Mg#$_{brucite}$=0.84) and slightly sequestered into/onto chrysotile (Mg#$_{chrysotile}$=0.93) compared to starting San-Carlos olivine. In our conditions a part of Fe^{3+} (not determined) might substitute to Si into the chrysotile. In our experiments, one general reaction of San Carlos olivine alteration can be written as follows:

$$2Mg_{1.8}Fe_{0.2}SiO_4 + 3H_2O = (Mg_{1-Z}Fe_Z)(OH)_2 + (Mg_{1-X}Fe_X)_3Fe_YSi_{2-Y}(OH)_4 \tag{1}$$
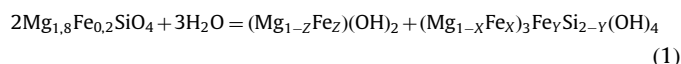
with $3X + Y \sim 0.24$ and $Z \sim 0.16$

This isochemical reaction implies a volume increase of $\sim 35\%$ (see discussion below).

On the XRD patterns (Fig. 1), characteristic peaks of chrysotile appear in the first hours or days of reaction, depending on the initial particle size of olivine (Fig. 1a and b). Secondary product growth rate is related to the variation of the crystal size with time. On the XRD patterns the full width at half maximum (FWHM) parameter for specific peaks, corresponding to a crystalline compound, can be directly associated to its coherent domain size when instrumental resolution function (IRF) and strain contribution are known. In our case, the FWHM for the plane (002) of chrysotile was used to obtain an estimation of the chrysotile size variation during the serpentinization process. Here, a decrease of FWHM implies an increase of coherent domain size as specified in the Scherrer equation. The FWHM variation with the reaction time reported in Fig. 1c shows a fast crystal growth step followed by a slow crystal growth step for chrysotile from 3 h to 30 days when starting grain size is $< 30\ \mu m$. Conversely, chrysotile coherent domain varies only moderately from 20 to 90 days for starting grain size $> 30\ \mu m$ (Fig. 1c). In this latter case, two explanations are possible: firstly, a preferential
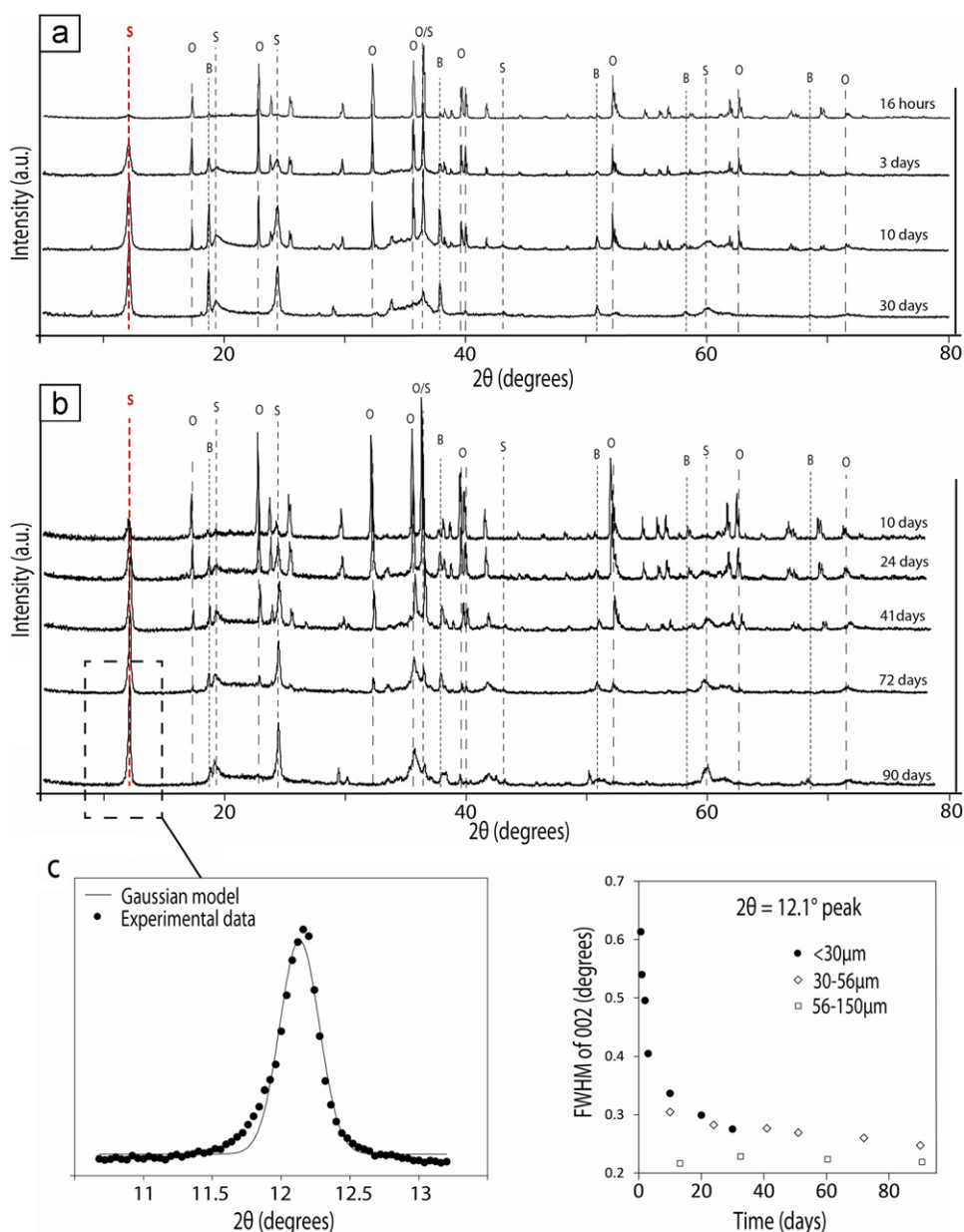
Fig. 1. XRD patterns following reaction advancement, (a) with starting grain size < 30 μm, (b) with starting grain size 30–56 μm, and (c) example of plot for the peak corresponding to bragg angle (2θ) of 12.1° and miller indice (002) with a gaussian deconvolution and plot of FWHM following reaction time for this peak. O: olivine, B: brucite and S: serpentine.

growth of other(s) crystal plane(s) than plane (002) is involved; secondly, dominant nucleation events promoting an increase of particle number concentration with time during mineral replacement of olivine can occur. FESEM observations support the first assumption because they have revealed a higher radial growth of tubular chrysotile for larger starting grain size (30–56 μm and 56–150 μm) at similar reaction time (Fig. 2f and h).

3.2. Determination of serpentinization rate

The time for complete olivine-to-serpentine transformation or complete serpentinization process depends on the starting grain size. For example, 30 days were required when starting grain size was < 30 μm while about 90 days were required for the 30–56 μm fraction (Fig. 1a and b). For 56–150 μm starting grain size, around 55% of mineral replacement was reached after 90 days of experiments.

Serpentinization rate of olivine was determined using a simple and novel method combining TGA and DTGA. TGA/DTGA was performed to quantify the molecular water (adsorbed or confined in pores) and hydroxyl groups (–OH) (incorporated in brucite and chrysotile) as illustrated in Fig. 3. In general, molecular water (H_2O) adsorbed or confined in pores onto mineral assemblage, was released at moderate temperature (< 200 °C). Conversely, the brucite and chrysotile minerals were dehydroxylated at higher temperatures. Here, a dehydroxylation peak closed to 370 °C was associated to brucite. This peak was shifted towards lower temperature, compared to the dehydroxylation of pure brucite peaking at 430 °C. This change of thermal stability was related to a significant incorporated amount of iron (Fe^{2+}) into brucite structure as recently claimed by Okamoto et al. [45]. Additionally we observed that weight loss ratio between serpentine and brucite is not constant following reaction advancement. Regarding the chrysotile, it was observed that it starts to be
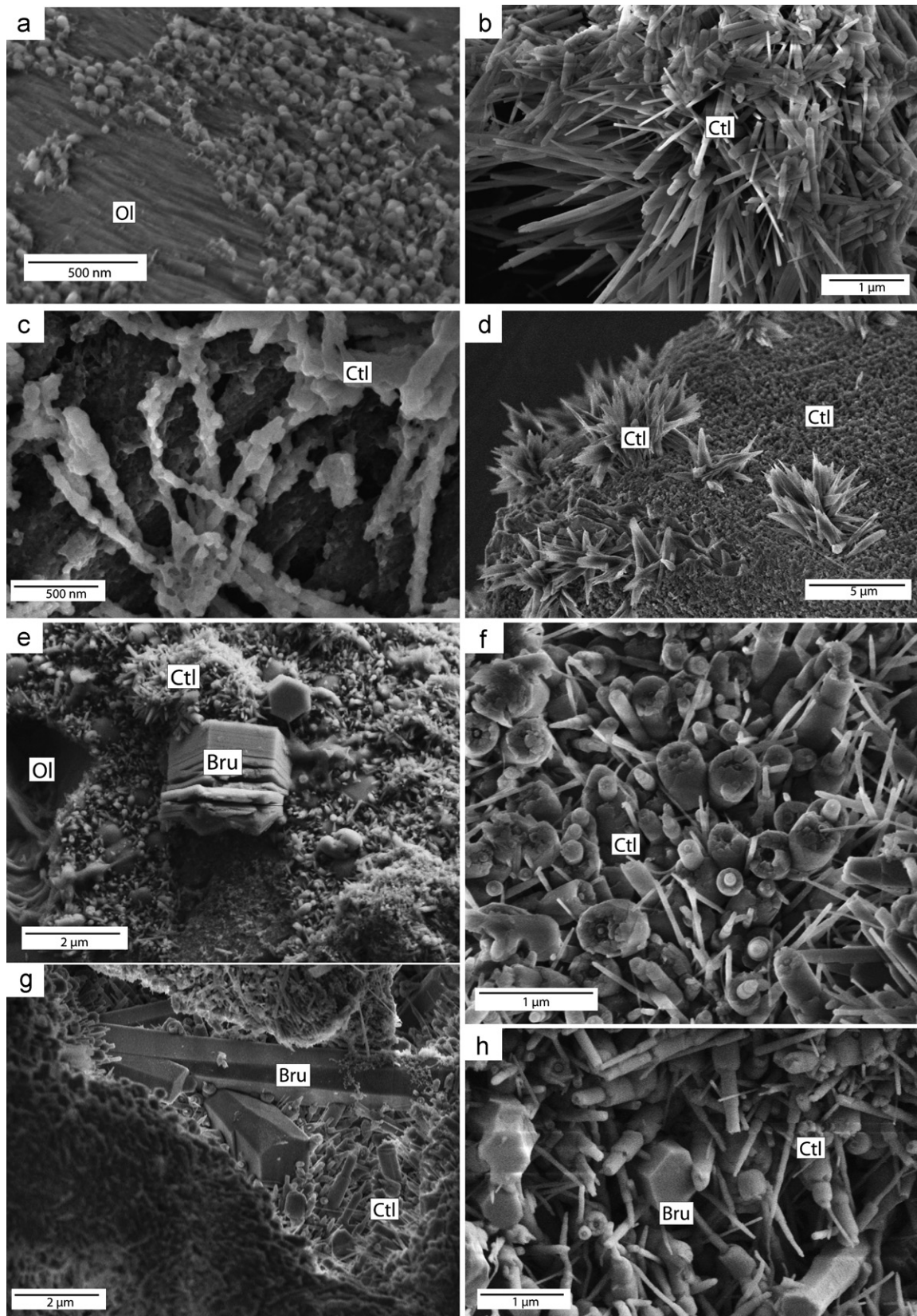
Fig. 2. Scanning electron microscope imaging of the experimental products. All shown experiments have been performed at pH=13.5 (at 25 °C) and 200 °C, for $< 30\,\mu m$ ((a), (b), (c) and (e)), 30–56 μm ((d), (f), and (g)) and 56–150 μm (h) grains size. (a) chrysotile and brucite nodules after 3 h of reaction (run no. 1), (b) chrysotile tube after 30 days of reaction (run no. 8) and (c) nodules aggregated in a tubular shape after 3 days of reaction (run no. 5). (d) Chrysotiles "bunch" at olivine grain surface after 10 days of reaction (run no. 13), (e) characteristic brucite/chrysotile assemblage after 30 days of reaction (run no. 6), (f) and (g) characteristic brucite/chrysotile assemblage and thick cylinder-in cylinder chrysotile after 90 days of reaction (run no. 18), and (h) characteristic brucite/chrysotile assemblage after 32 days of reaction (run no. 20). Bru: brucite, Ctl: chrysotile, and Ol: olivine.
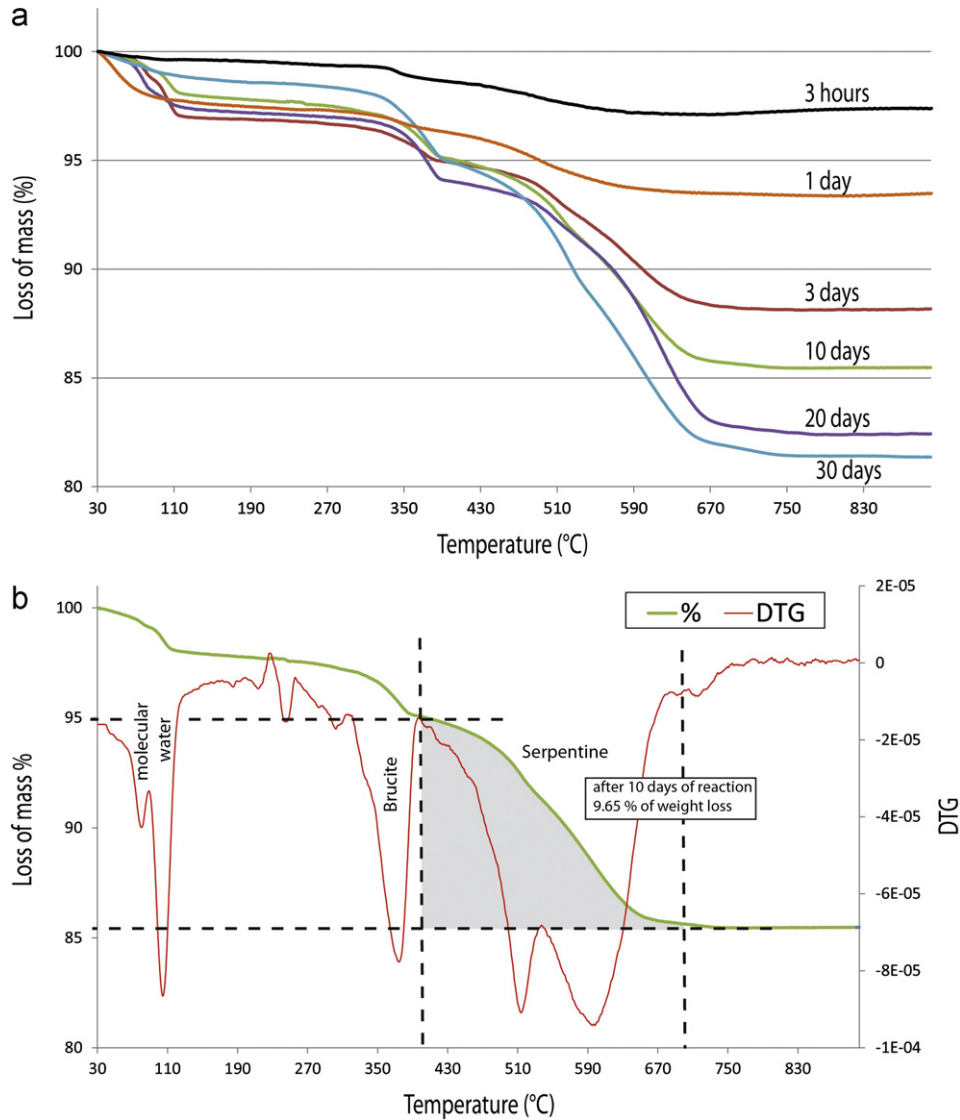
Fig. 3. (a) Thermogravimetric analyses (TGA) for experiments of 3 h to 30 days (run no. 1, 3, 5, 6, 7 and 8) with grains $< 30\,\mu m$, and (b) focus and decomposition of TGA and DTG corresponding spectra after 10 days of reaction.

dehydroxylated at about 400 °C and it was completely dehydroxylated at approximately 700 °C for most of the experiments. In several cases, two typical dehydroxylation episodes were measured at 515 and 600 °C. We note that the starting dehydroxylation step for chrysotile can be overlapped with residual –OH from dehydroxylation of brucite, possibly producing a slight over-estimation of incorporated –OH into the chrysotile phase. This direct measurement was used to calculate the serpentinization extent (%) at a given reaction time as follows:

$$\xi_t = ((-OH)_{measured}/(-OH)_{theoretical})*100 \qquad (2)$$

where $(-OH)_{theoretical}$ is the theoretical weight (in %) of hydroxyl groups incorporated in chrysotile (400 °C–700 °C) with a chemical formula simplified to $Mg_3Si_2O_5(OH)_4$ for the $(-OH)_{theoretical}$ considered. Then, the serpentinization extent was correlated with reaction time (ξ_t vs. t). These experimental-calculated data are displayed in Fig. 4. As previously stated, a complete serpentinization extent was determined after 30 days for smaller olivine grains ($< 30\,\mu m$) and after 90 days for intermediate olivine grains ($30 < $ grain size < 56). These results clearly show that the serpentinization rate strongly depends on the starting grain size of olivine. This explains why for larger olivine grains ($56 < $ grain
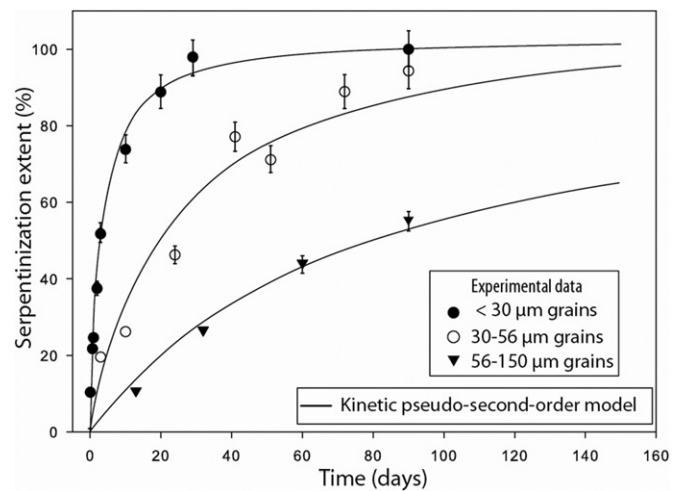

Fig. 4. Serpentinization degree versus time for the hydration reaction at different grain sizes for $T=200$ °C, $P_{sat}=1.6$ Mpa and fluid/solid$=15$. Maximum error bars corresponding to 5% of the serpentinization extent calculated was also reported. Data were fitted using a kinetic pseudo-second-order model.

size $<150\,\mu m$), about 55% of serpentinization extent was only reached after 90 days of olivine–fluid interactions.

Experimental data reported in Fig. 4 were fitted using a kinetic pseudo-second-order model. This simple kinetic model describes a fast serpentinization step followed by a slow serpentinization step until an asymptotic maximum with time. Its integrated form

can be expressed as follows:

$$\xi_t = \frac{\xi_{max}t}{t_{1/2}+t} \tag{3}$$

where ξ_t, is the serpentinization extent for a given reaction time t, ξ_{max} is the maximum serpentinization extent (close to 100% for a complete serpentinization) and $t_{1/2}$ is the half serpentinization time. The fast serpentinization step can be associated to the fast dissolution of smaller olivine grains initially far from equilibrium, but the dissolution process was spatially and temporally coupled to a fast precipitation of chrysotile and brucite. For this reason, the external shape of starting olivine grains (primary or parent mineral) was preserved, leading to a porous granular material composed of chrysotile and brucite minerals when complete mineral replacement of olivine was reached. Finally, the mineral replacement initial-rate ν_0 (or serpentinization initial-rate) was defined as the slope of the tangent line when time t tends toward zero on the r vs t curve. Analytically, $\nu_0=(\xi_{max}/t_{1/2})$ and it varies

Table 2
Summary of kinetic parameters obtained from the pseudo-second-order model.

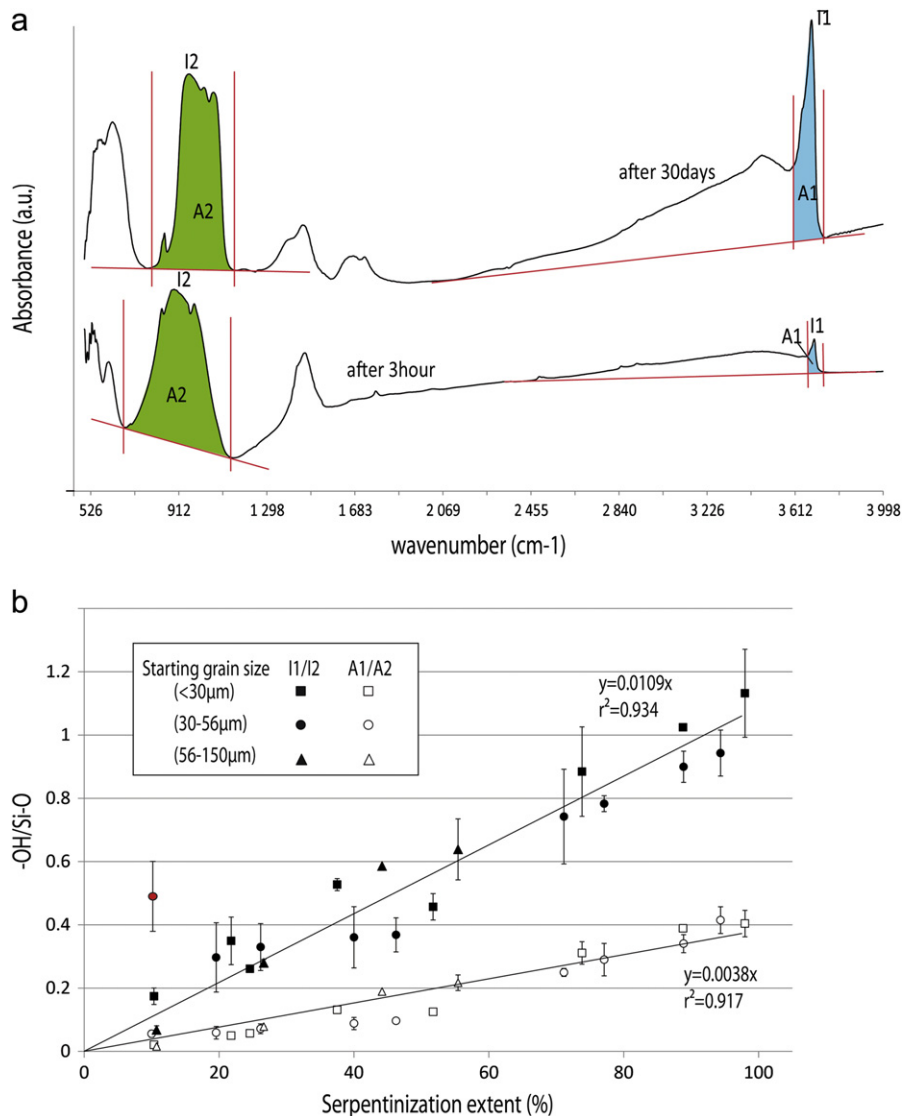| Initial particule size of olivine (µm)	ξ_{max} (%)		$t_{1/2}$ (days)	Initial rate (1/s)	Fitting r^2
	Exp.	Calc.			
<30	97.96	100 ± 1.7	3.2 ± 0.3	$3.62-06\pm0.35E-06$	0.989
30–56	94.35	100 ± 8.5	23.1 ± 5.3	$5.01E-07\pm0.9E-07$	0.947
56–150	55.4	100 ± 16	79 ± 21	$1.46E-07\pm0.2E-07$	0.981

Fig. 5. (a) Transmission spectra (in absorbance) for starting grain size $<30\,\mu m$ after 3 h (run no. 1) and 30 days (run no. 8) of reaction with corresponding base line and range employed for treatment. Blue area corresponds to –OH band integration A1 with maximum intensity I1, green area corresponds to Si–O band integration A2 with maximum intensity I2. (b) Corresponding –OH/Si–O ratio: A1/A2 and I1/I2 following serpentinization advancement determined by TG and DTG analysis, square, triangle and circles correspond respectively to experiments for $<30\,\mu m$, 30–56 µm and 56–150 µm starting grain size fraction (empty for A1/A2 and black for I1/I2) with corresponding standard deviation, black line corresponds to the best linear regression with the exclusion of red point. (For interpretation of the references to color in this figure legend, the reader is referred to the web version of this article.)

from $3.6 \times 10^{-6}\,s^{-1}$ to $1.4 \times 10^{-7}\,s^{-1}$ at 200 °C respectively for $< 30\,\mu m$ grain size and 56–150 μm grain size. Full serpentinization was not obtained experimentally on $56 < $ particle size $< 150\,\mu m$ but the theoretical model presented predicts a close to complete serpentinization ($> 90\%$) around 2 years.

Indeed, the fluid/olivine interface depending on the initial olivine grain size is the main factor controlling the initial rate. These kinetic parameters concerning the three different size classes of olivine and respective correlation factors are summarized in Table 2.

The uncertainties of the TG-method result from the calculation method. The main approximation is the systematic consideration of the same temperature range (400–700 °C). Considering all the experiments, a variation of the temperature range of ± 50 °C will only induce a difference of 1%–5% for the final serpentinization calculated advancement. Based on this calculation we assure that the maximum uncertainty of the proposed methods is around 5% as reported in Fig. 4. The uncertainty on the calculated initial rate is directly depending on the standard deviation obtained for $t_{1/2}$ and ξ_{max} (Table 2).

In a complementary way, the transmission FTIR spectra were obtained. Characteristic stretching bands for hydroxyl group (–OH) in chrysotile–brucite and for Si–O group in olivine–chrysotile were used. Particularly, the relative (–OH)/(Si–O) ratio
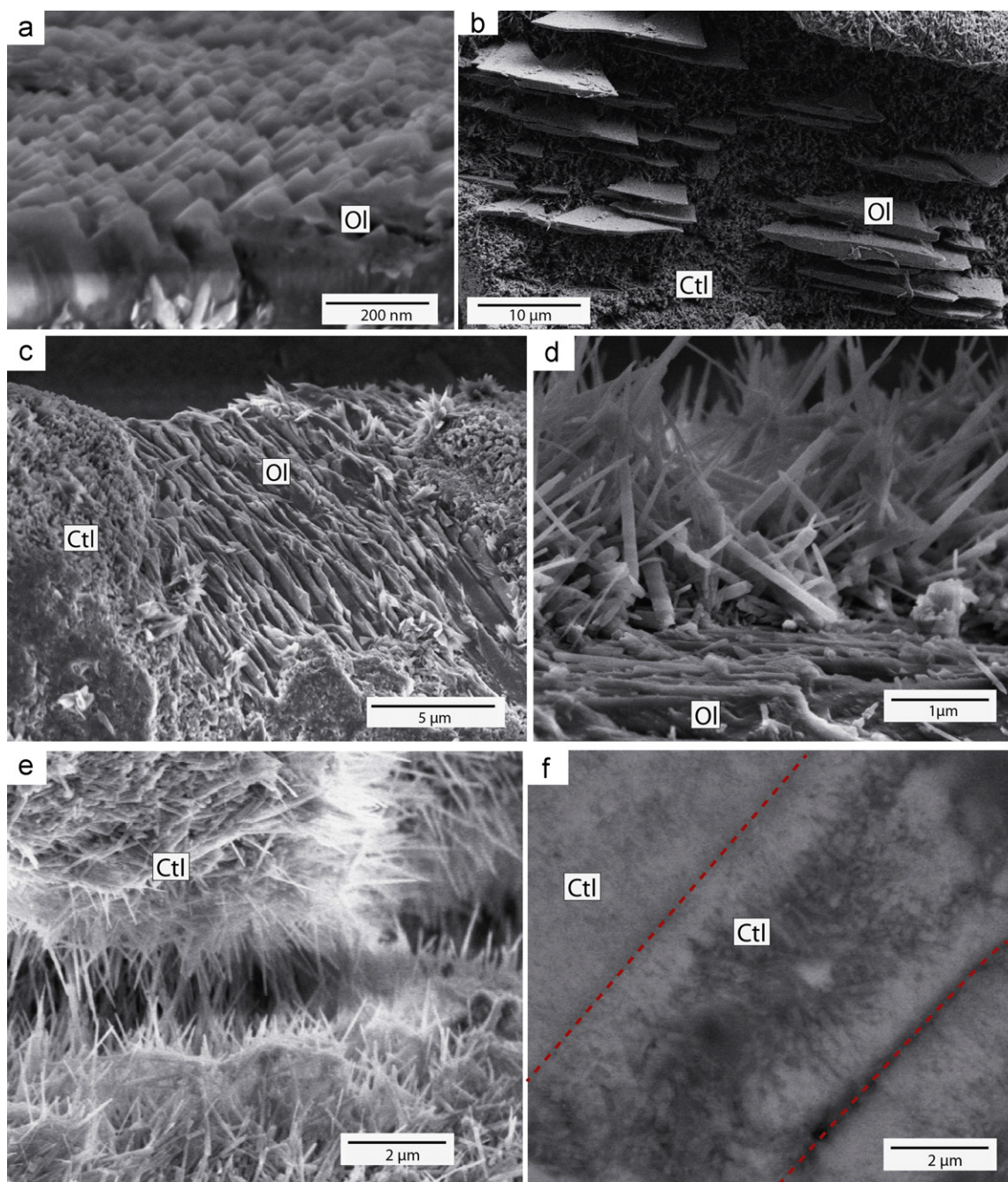

Fig. 6. Scanning electron microscope imaging of the experimental products for starting grain size $< 30\,\mu m$ (a), 30–56 μm (c–f) and 56–150 μm (b). (a) etch pits at olivine grain surface after 3 days (run no. 5), (b) dissolution notches after 32 days of reaction (run no. 20), (c) dissolution notches after 24 days of reaction (run no. 14), (d) chrysotile micro-tubes at olivine grain surface after 3 days of reaction (run no. 12), (e) contact between two olivine grains and (f) microfracturing in section after 10 days of reaction (run no. 13). Red dotted lines represent initial border of the supposed crack. Ctl: chrysotile and Ol: olivine. (For interpretation of the references to color in this figure legend, the reader is referred to the web version of this article.)

using integrated bands' intensities or maximum band intensities was correlated with the serpentinization extent deduced from TG/DTG analyses (Fig. 5). This gives two calibration curves that can be used to determine serpentinization rate using FTIR measurements. However, FTIR measurements should be taken with caution because of the overlapping of –OH (for brucite and serpentine) and Si–O groups (for serpentine and olivine). We could overcome this problem if serpentine/brucite produced molar ratio stayed constant following reaction time, but as described before it is not the case. Here, we conclude that the TG/DTG analyses are a powerful tool to determine the mineral replacement rate of olivine by chrysotile–brucite mineral assemblage. For this specific case, the FTIR measurements provide first information about the olivine serpentinization extent.

This study confirms that the serpentinization rate is enhanced by high alkaline conditions. Serpentinization rate has been studied for a large variety of experimental conditions under neutral conditions [33–40,46]. For comparison, serpentinization extent of 50–100 μm starting grain size at 200 °C reached only ~20% after ~4 months under neutral conditions [38]. This corresponds to a kinetic 5 times slower to our results on the largest starting grain size (56–150 μm).

3.3. Serpentinization steps and reaction mechanism

The first step of reaction in alkaline medium is characterized by a fast dissolution of olivine associated to the formation of preferential dissolution features as notches and etch pits (Fig. 6a–c) [47–49]. Conjointly, precipitation of the first clusters of brucite and chrysotile occur at the olivine surface. FESEM observations have revealed the preservation of olivine shape after complete serpentinization (Fig. 7). This suggests that olivine alteration invokes coupled dissolution–precipitation processes

[28]. Despite ultrasonic treatment and dispersion on ethanol (up to 1 h 30 min), which can easily break up the new brucite/chrysotile mineral assemblage, the shape and size of olivine grains are always preserved regardless the completion of the reaction. Based on these results, we assume a higher super-saturation of solution with respect to chrysotile tubes at the olivine–solution interfaces. Super-saturation at olivine–alkaline solution interfaces allows rapid heterogeneous serpentine nucleation as small nodules of chrysotile and brucite (Fig. 2a). This nucleation phase is followed by a phase of epitaxial growth of chrysotile and brucite forming a porous medium (Fig. 6d–f). Chrysotile grows as elongated tubes with various morphology (conical, cylinder in cylinder) with a size depending on starting olivine grain size. Largest starting grain size induces smallest reacting surface and thus slower kinetic of alteration and formation of largest chrysotiles' particles. Olivine grain size influenced initial dissolution rate v_0, passivation state and general kinetic of alteration.

Serpentinization reaction is then favored by the formation of notches connected to a micro-fracturing network inside olivine (e.g. 32 days of reaction for > 30 μm grains; Fig. 6b and c). This micro-fracturing network might start following ordered families of fine-scale fractures from olivine grains [44]. In the oceanic crust, the micro-fracturing may be attributed to the stress generated by the volume increase during olivine serpentinization [28]. In our free fluid system, there is no evident expansion during olivine replacement. Volume increase due to olivine serpentinization (35%) is likely accounted by material loss in solution, but it could also cause the micro-fracturing [28,50]. With the formation of smaller sub-grains, micro-fracturing allows an easier fluid percolation and increase the total reaction-surface (Fig. 6e and f). This process permits a continuous and total replacement of olivine by chrysotile and brucite as summarized in Fig. 8. This is in
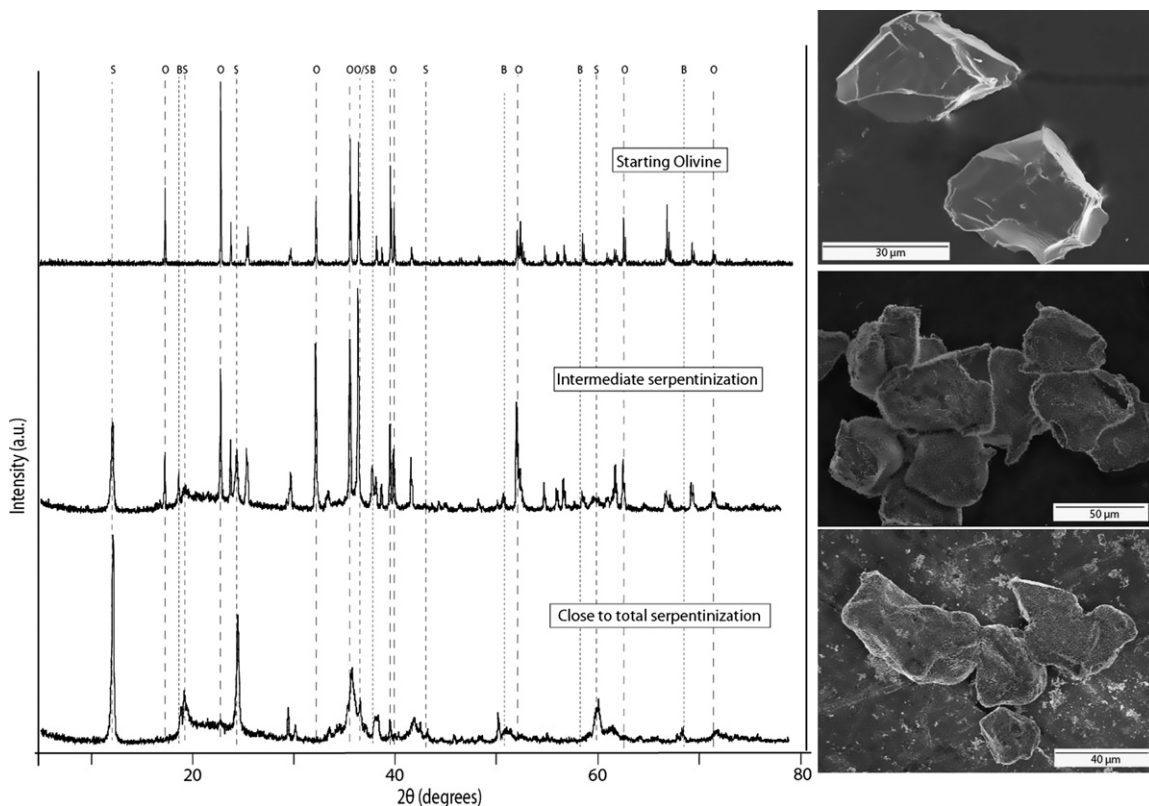

Fig. 7. XRD pattern and corresponding scanning electron microphotography from pure starting San Carlos olivine to close to 100% of replacement by serpentine and brucite. Note the preservation of the olivine grains dimension and shape. S: serpentine, B: brucite, and O: olivine.
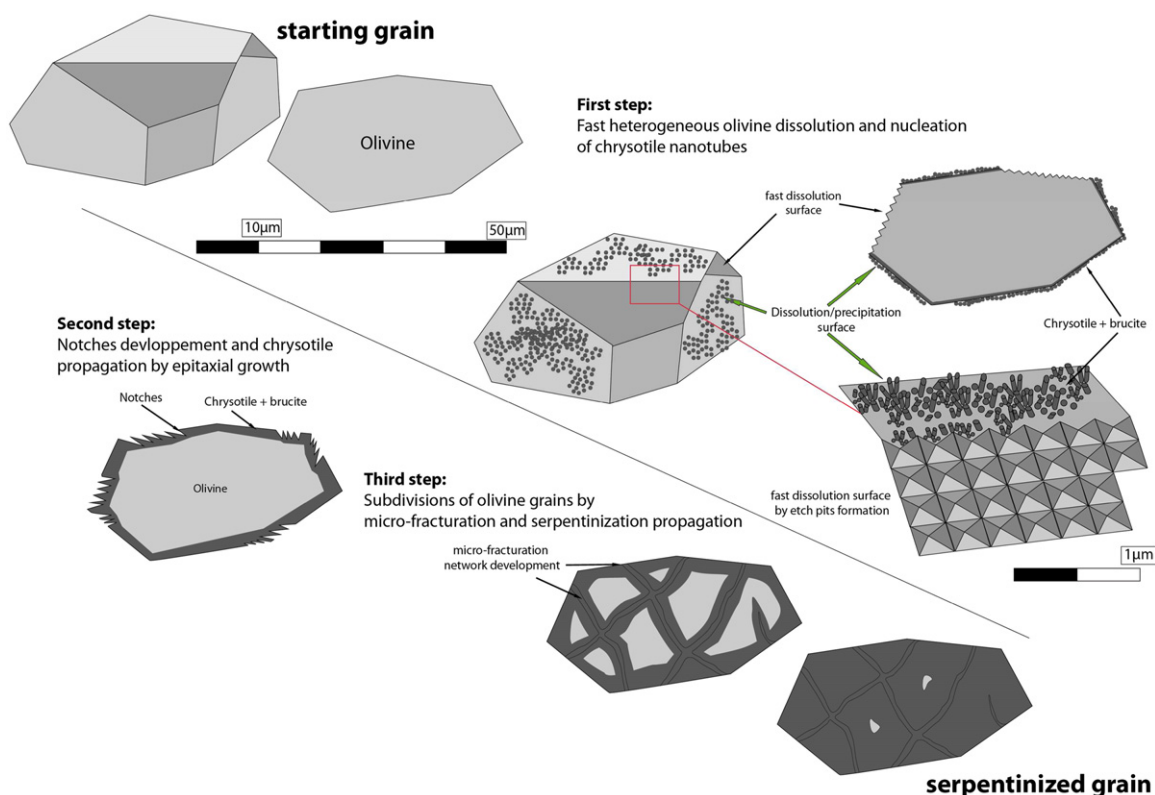
Fig. 8. Schematic synthesis presenting the different steps of olivine replacement by chrysotile and brucite.

agreement with natural observation and development of mesh type texture described in natural rocks [26–28,50–52]. In this case, the fluid can percolate slowly until a complete mineral replacement. In others cases, the formation of a protective layer would induce a non-continuous passivation process by blocking intra-particles diffusion and the reaction can be stopped before its complete achievement [53]. Mass transfer will play a major role for the preservation of volume and shape of starting olivine grain.

4. Conclusion

Olivine alteration was investigated under alkaline conditions for different starting grain sizes at 200 °C. In this study, we were able to follow complete olivine replacement by an assemblage of chrysotile and brucite.

Thermogravimetric analyses were used to investigate the dehydroxylation of hydrated phases and thus the serpentinization extent as a function of time. Based on this innovative approach, we were able to estimate punctually the serpentinization advancement and a kinetic pseudo-second-order model was used to describe experimental data. This could allow a prediction of reaction advancement for the largest starting grain size.

We also established two calibration curves between the –OH/Si–O bands measured in FTIR and the degree of serpentinization. This enables to have an estimation of the kinetic rates of serpentinization directly from the FTIR spectra analysis. This must be considered with caution because of the overlapping of –OH bands between brucite and serpentine.

Under our experimental conditions, olivine is replaced by chrysotile and brucite by coupled dissolution–precipitation processes. Fast dissolution of olivine, preferential dissolution features formation and process of grain subdivisions by fracturing are involved to explain a complete mineral replacement of olivine.

This implies the preservation of external shape of olivine grains as typically observed in natural systems.

Appendix A. Supplementary material

Supplementary data associated with this article can be found in the online version at doi:10.1016/j.jcrysgro.2012.02.040.

References

[1] F. Deschamps, S. Guillot, M. Godard, C. Chauvel, M. Andreani, K. Hattori, In situ characterization of serpentinites from forearc mantle wedges: timing of serpentinization and behavior of fluid-mobile elements in subduction zones, Chemical Geology 269 (2010) 262–277.
[2] K. Hattori, S. Guillot, Volcanic fronts form as a consequence of serpentinite dehydration in the forearc mantle wedge, Geology 31 (2003) 525–528.
[3] K. Hattori, S. Guillot, Geochemical character of serpentinites associated with high- to ultrahigh-pressure metamorphic rocks in the Alps, Cuba, and the Himalayas: recycling of elements in subduction zones, Geochemistry Geophysics Geosystems 8 (2007).
[4] C.-T.A. Lee, M. Oka, P. Luffi, A. Agranier, Internal distribution of Li and B in serpentinites from the Feather River Ophiolite, California, based on laser ablation inductively coupled plasma mass spectrometry, Geochemistry Geophysics Geosystems 9 (2008) Q12011.

[5] T.M. McCollom, E.L. Shock, Fluid–rock interactions in the lower oceanic crust: thermodynamic models of hydrothermal alteration, Journal of Geophysical Research 103 (1998) 547–575.

[6] F. Vils, L. Pelletier, A. Kalt, O. Müntener, T. Ludwig, The lithium, boron and beryllium content of serpentinized peridotites from ODP Leg 209 (Sites 1272A and 1274A): implications for lithium and boron budgets of oceanic lithosphere, Geochimica et Cosmochimica Acta 72 (2008) 5475–5504.

[7] F. Deschamps, S. Guillot, M. Godard, M. Andreani, K. Hattori, Serpentinites act as sponges for fluid-mobile-elements in abyssal and subduction zone environments, Terra Nova 23 (2011) 171–178.

[8] S. Guillot, K.H. Hattori, J. de Sigoyer, T. Nagler, A.-L. Auzende, Evidence of hydration of the mantle wedge and its role in the exhumation of eclogites, Earth and Planetary Science Letters 193 (2001) 115–127.

[9] A. Bloise, E. Belluso, E. Fornero, C. Rinaudo, E. Barrese, S. Capella, Influence of synthesis conditions on growth of Ni-doped chrysotile, Microporous and Mesoporous Materials 132 (2010) 239–245.

[10] A. Bloise, E. Belluso, E. Barrese, D. Miriello, C. Apollaro, Synthesis of Fe-doped chrysotile and characterization of the resulting chrysotile fibers, Crystal Research and Technology 44 (2009) 590–596.

[11] A. Bloise, E. Barrese, C. Apollaro, Hydrothermal alteration of Ti-doped forsterite to chrysotile and characterization of the resulting chrysotile fibers, Neues Jahrbuch für Mineralogie-Abhandlungen 185 (2009) 297–304.

[12] E. Korytkova, L. Pivovarova, V. Gusarov, Influence of iron on the kinetics of formation of chrysotile nanotubes of composition $(Mg, Fe)_3Si_2O_5(OH)_4$ under hydrothermal conditions, Geochemistry International 45 (2007) 825–831.

[13] A. McDonald, B. Scott, G. Villemure, Hydrothermal preparation of nanotubular particles of a 1:1 nickel phyllosilicate, Microporous and Mesoporous Materials 120 (2009) 263–266.

[14] B. Wunder, F. Deschamps, A. Watenphul, S. Guillot, A. Meixner, R. Romer, et al., The effect of chrysotile nanotubes on the serpentine-fluid Li-isotopic fractionation, Contributions to Mineralogy and Petrology 159 (2010) 781–790.

[15] G. Falini, E. Foresti, I.G. Lesci, B. Lunelli, P. Sabatino, N. Roveri, Interaction of bovine serum albumin with chrysotile: spectroscopic and morphological studies, Chemistry: A European Journal 12 (2006) 1968–1974.

[16] A.F. Gualtieri, M.L. Gualtieri, M. Tonelli, In situ ESEM study of the thermal decomposition of chrysotile asbestos in view of safe recycling of the transformation product, Journal of Hazardous Materials 156 (2008) 260–266.

[17] E. Foresti, E. Fornero, I.G. Lesci, C. Rinaudo, T. Zuccheri, N. Roveri, Asbestos health hazard: a spectroscopic study of synthetic geoinspired Fe-doped chrysotile, Journal of Hazardous Materials 167 (2009) 1070–1079.

[18] P. Sabatino, L. Casella, A. Granata, M. Iafisco, I.G. Lesci, E. Monzani, et al., Synthetic chrysotile nanocrystals as a reference standard to investigate surface-induced serum albumin structural modifications, Journal of Colloid and Interface Science 314 (2007) 389–397.

[19] A. Beinlich, H. Austrheim, J. Glodny, M. Erambert, T.B. Andersen, CO_2 sequestration and extreme Mg depletion in serpentinized peridotite clasts from the Devonian Solund basin, Geochimica et Cosmochimica Acta 74 (2010) 6935–6964.

[20] F. Larachi, I. Daldoul, G. Beaudoin, Fixation of CO_2 by chrysotile in low-pressure dry and moist carbonation: ex-situ and in-situ characterizations, Geochimica et Cosmochimica Acta 74 (2010) 3051–3075.

[21] T.M. McCollom, J.S. Seewald, A reassessment of the potential for reduction of dissolved CO_2 to hydrocarbons during serpentinization of olivine, Geochimica et Cosmochimica Acta 65 (2001) 3769–3778.

[22] T. Yajima, T. Ohsumi, Y. Mizuochi, A. Ninomiya, T. Kato, Field Study on Co₂ Fixation by Serpentinite Rock-Bed, Dans: Greenhouse Gas Control Technologies, vol. 7, Elsevier Science Ltd, Oxford, 2005, p. 2027–2030.

[23] P. Beck, E. Quirico, G. Montes-Hernandez, L. Bonal, J. Bollard, F.-R. Orthous-Daunay, et al., Hydrous mineralogy of CM and CI chondrites from infrared spectroscopy and their relationship with low albedo asteroids, Geochimica et Cosmochimica Acta 74 (2010) 4881–4892.

[24] M. Andreani, A. Baronnet, A.-M. Boullier, J.-P. Gratier, A microstructural study of a "crack-seal" type serpentine vein using SEM and TEM techniques, European Journal of Mineralogy 16 (2004) 585–595.

[25] M. Andreani, C. Mével, A.-M. Boullier, J. Escartin, Dynamic control on serpentine crystallization in veins: constraints on hydration processes in oceanic peridotites, Geochemistry Geophysics Geosystems 8 (2007) Q02012.

[26] F.J. Wicks, E.J.W. Whittaker, Serpentine textures and serpentinization, Canadian Mineralogist 15 (1977) 459–488.

[27] B. Evans, The serpentinite multisystem revisited: chrysotile is metastable, International Geology Review 46 (2004) 479–506.

[28] A. Putnis, Mineral replacement reactions, Reviews in Mineralogy and Geochemistry 70 (2009) 87–124.

[29] A. Putnis, C.V. Putnis, The mechanism of re-equilibration of solids in the presence of a fluid phase, Journal of Solid State Chemistry 180 (2007) 1783–1786.

[30] A. Putnis, Mineral replacement reactions: from macroscopic observations to microscopic mechanisms, Mineralogical Magazine 66 (2002) 689–708.

[31] D.S. Kelley, J.A. Karson, D.K. Blackman, G.L. Früh-Green, D.A. Butterfield, M.D. Lilley, et al., An off-axis hydrothermal vent field near the Mid-Atlantic Ridge at 30° N, Nature 412 (2001) 145–149.

[32] K.A. Ludwig, D.S. Kelley, D.A. Butterfield, B.K. Nelson, G. Früh-Green, Formation and evolution of carbonate chimneys at the Lost City Hydrothermal Field, Geochimica et Cosmochimica Acta 70 (2006) 3625–3645.

[33] D.E. Allen, W.E. Seyfried, Compositional controls on vent fluids from ultramafic-hosted hydrothermal systems at mid-ocean ridges: an experimental study at 400 °C, 500 bars, Geochimica et Cosmochimica Acta 67 (2003) 1531–1542.

[34] A.H. Macdonald, W.S. Fyfe, Rate of serpentinization in seafloor environments, Tectonophysics 116 (1985) 123–135.

[35] C. Marcaillou, M. Muñoz, O. Vidal, T. Parra, M. Harfouche, Mineralogical evidence for H_2 degassing during serpentinization at 300 °C/300 bar, Earth and Planetary Science Letters 303 (2011) 281–290.

[36] B. Martin, W.S. Fyfe, Some experimental and theoretical observations on the kinetics of hydration reactions with particular reference to serpentinization, Chemical Geology 6 (1970) 185–202.

[37] W.E. Seyfried Jr, W.E. Dibble Jr, Seawater–peridotite interaction at 300 °C and 500 bars: implications for the origin of oceanic serpentinites, Geochimica et Cosmochimica Acta 44 (1980) 309–321.

[38] W.E. Seyfried Jr., D.I. Foustoukos, Q. Fu, Redox evolution and mass transfer during serpentinization: an experimental and theoretical study at 200 °C, 500 bar with implications for ultramafic-hosted hydrothermal systems at Mid-Ocean Ridges, Geochimica et Cosmochimica Acta 71 (2007) 3872–3886.

[39] W.W. Wegner, W.G. Ernst, Experimentally determined hydration and dehydration reaction rates in the system MgO–SiO2–H2O, American Journal of Science 283A (1983) 151–180.

[40] K. Yada, K. Iishi, Growth and microstructure of synthetic chrysotile, American Mineralogist 62 (1977) 958–965.

[41] A. Baronnet, B. Devouard, Topology and crystal growth of natural chrysotile and polygonal serpentine, Journal of Crystal Growth 166 (1996) 952–960.

[42] K. Yada, K. Iishi, Serpentine minerals hydrothermally synthesized and their microstructures, Journal of Crystal Growth 24–25 (1974) 627–630.

[43] W.E. Seyfried Jr., D.I. Foustoukos, Q. Fu, Redox evolution and mass transfer during serpentinization: an experimental and theoretical study at 200 °C, 500 bar with implications for ultramafic-hosted hydrothermal systems at Mid-Ocean Ridges, Geochimica et Cosmochimica Acta 71 (2007) 3872–3886.

[44] C. Normand, A.E. Williams-Jones, R.F. Martin, H. Vali, Hydrothermal alteration of olivine in a flow-through autoclave: nucleation and growth of serpentine phases, American Mineralogist 87 (1699 –1709).

[45] A. Okamoto, Y. Ogasawara, Y. Ogawa, N. Tsuchiya, Progress of hydration reactions in olivine–H₂O and orthopyroxenite–H₂O systems at 250 °C and vapor-saturated pressure, Chemical Geology 289 (2011) 245–255.

[46] M. Bentabol, M.D. Ruiz Cruz, F.J. Huertas, Hydrothermal synthesis (200 °C) of Co–kaolinite and Al–Co–serpentine, Applied Clay Science 42 (2009) 649–656.

[47] J. Hövelmann, H. Austrheim, A. Beinlich, I. Anne Munz, Experimental study of the carbonation of partially serpentinized and weathered peridotites, Geochimica et Cosmochimica Acta 75 (2011) 6760–6779.

[48] A. Awad, A.F. Koster van Groos, S. Guggenheim, Forsteritic olivine: effect of crystallographic direction on dissolution kinetics, Geochimica et Cosmochimica Acta 64 (2000) 1765–1772.

[49] M.A. Velbel, J.M. Ranck, Etch pits on naturally altered olivine from dunites of the Appalachian Blue Ridge Mountains, North Carolina, USA, Mineralogical Magazine 72 (2008) 145–148.

[50] A. Putnis, H. Austrheim, Fluid-induced processes: metasomatism and metamorphism, Geofluids 10 (2010) 254–269.

[51] F.J. Wicks, E.J.W. Whittaker, J. Zussman, An idealized model for serpentine textures after olivine, The Canadian Mineralogist 15 (1977) 446–458.

[52] J.B. Moody, Serpentinization: a review, Lithos 9 (1976) 125–138.

[53] G. Montes-Hernandez, A. Pommerol, F. Renard, P. Beck, E. Quirico, O. Brissaud, In situ kinetic measurements of gas–solid carbonation of $Ca(OH)_2$ using an infrared microscope coupled to a reaction cell, Chemical Engineering Journal 161 (2010) 250–256.

[54] B. Malvoisin, F. Brunet, J. Carlut, S. Rouméjon, M. Cannat, Serpentinization of oceanic peridotites: 2. Kinetics and processes of San Carlos olivine hydrothermal alteration, J. Geophys. Res., doi:10.1029/2011JB008842, in press.